

# Wave Reflections in Excitable Media Using Morris-Lecar Dynamics

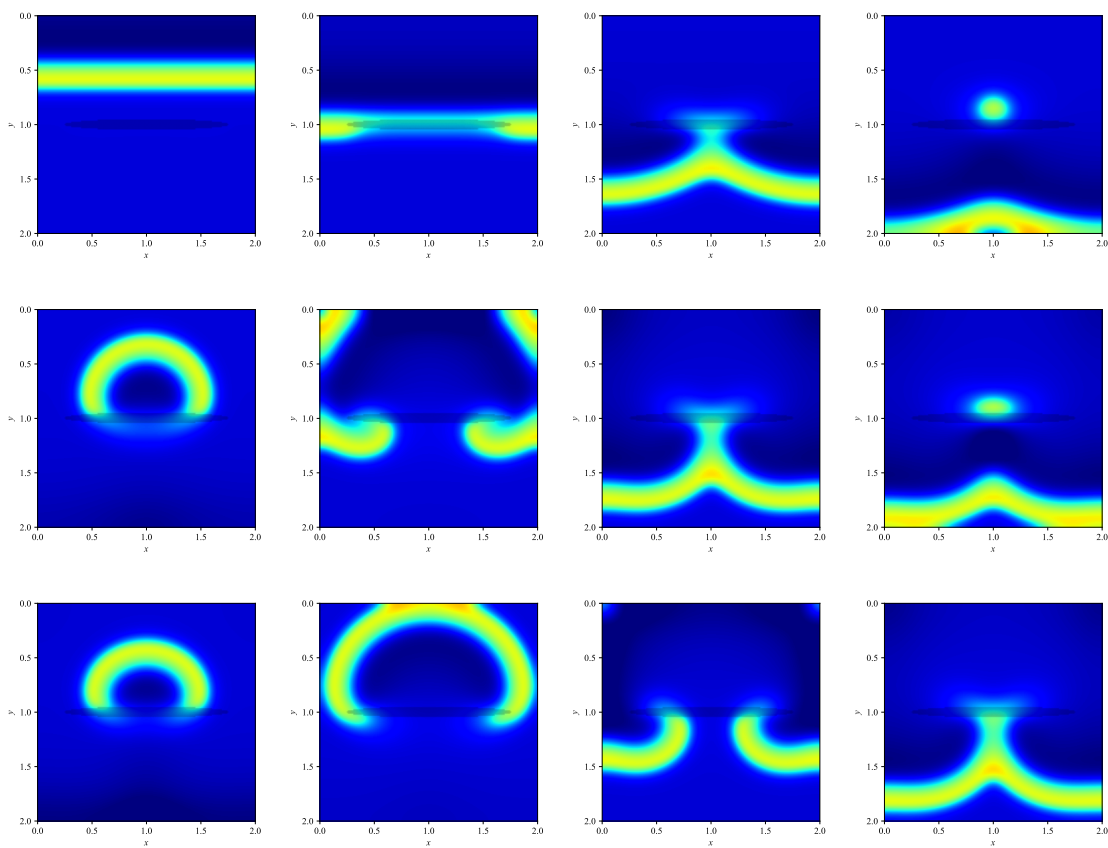
Vincent Lovero

University of California Davis  
Program: Applied Mathematics  
Senior Thesis

---

Faculty Advisor: Timothy J. Lewis

June, 2020



# 1 Introduction

Excitable media are ubiquitous in nature, and are often found in biological, physical, and chemical systems. An excitable medium is a spatially distributed dynamical system, where each elementary segment exhibits threshold dynamics. These neighboring segments locally interact via a diffusive transport process allowing for excitation to be passed from one segment to the next by this local coupling. When a perturbation of sufficient magnitude is applied to an excitable medium in a resting state, the system undergoes a “self-activating” reaction before returning back to rest. If a stimulus of inadequate size is applied, the system does not deviate much from its resting state and returns to rest.

A natural response to an adequate stimulus is the development of a wave of excitation; like when a match is dropped into a field of dried grass, the small perturbation quickly turns into a wavefront of burning grass that quickly spreads before dying out due to a lack of grass to burn. However, there is also less common esoteric behaviors. An example of unusual behavior in excitable media is a one-dimensional spiral wave. The one-dimensional spiral wave describes a circulating wave used to describe reentry. The underlying mechanisms of one-dimensional spiral waves are unclear and the conditions that promote their existence. One-dimensional spiral waves have been tied to life-threatening arrhythmias of the heart, and thus gaining insight on the conditions that promote their existence can serve to be useful.

Here we explore the Morris-Lecar model in excitable media in both one and two spatial dimensions, searching for conditions that promote wave reflections. Heterogeneous domains—non-excitable region(s) that exist in the same domain as the excitable medium—are used to search for reflections. Furthermore, analogous behavior in coupled cells is also studied.

## 2 The Morris-Lecar Model and Dynamics

The Morris-Lecar (ML) model is a two-variable biophysical model that describes the electrophysiological dynamics of muscle cells from a barnacle [6]. Despite the fact that it was originally developed for barnacle muscle, it captures the essential excitable (i.e., threshold and recovery) dynamics, as well as the basic biophysical mechanisms, of both cardiac cells and neurons, and therefore it is often used as a canonical model for these cells. Below, we describe the ML model, and examine its properties along with the basic dynamics.

The ML equations are,

$$C \frac{dV}{dt} = -g_{Ca}m_{\infty}(V)(V - E_{Ca}) - g_K W(V - E_K) - g_l(V - E_l) + I_{ext} = f(V, W) \quad (2.1)$$

$$\frac{dW}{dt} = \phi \frac{w_{\infty}(V) - W}{\tau(V)} = \phi g(V, W) \quad (2.2)$$

where,

$$m_{\infty}(V) = \frac{1}{2} \left( 1 + \tanh \frac{V - V_1}{V_2} \right) \quad (2.3)$$

$$w_{\infty}(V) = \frac{1}{2} \left( 1 + \tanh \frac{V - V_3}{V_4} \right) \quad (2.4)$$

$$\tau(V) = \left( \cosh \frac{V - V_3}{2V_4} \right)^{-1} \quad (2.5)$$

Equation (2.1) is a balance of three types of ion channel currents: calcium  $I_{Ca} = g_{Ca}m_{\infty}(V)(V - E_{Ca})$ , potassium  $I_K = g_K w(V - E_K)$ , and leakage  $I_l = g_l(V - E_l)$ .  $V$  represents the membrane potential or voltage,  $C$  is the membrane capacitance,  $I_{ext}$  is the applied current.  $g_{Ca}$ ,  $g_K$ , and  $g_l$  are the peak conductance equilibria for the calcium, potassium, and leakage currents respectively.  $E_{Ca}$ ,  $E_K$ , and  $E_l$  are the equilibrium potentials. Equation (2.2) describes how ion channels are opening and closing, or more specifically, determining whether or not the potassium ion channel is in a conducting or a non-conducting state.  $W$  is the probability that the potassium ion channel is open. We often refer to this variable as the “recovery” variable. In both equations (2.1) and (2.2), there are voltage-dependent probability distribution functions (2.3) and

(2.4): for a fixed value  $V$ ,  $m_\infty$  represents the probability that calcium ion channels are open, and similarly  $w_\infty$  is the probability that the potassium channels are open.  $\tau(V)/\phi$  is the  $V$ -dependent, time constant for the relaxation of  $W$ . Unless otherwise specified, the nondimensionalized parameters used throughout this paper are,

|          |      |           |       |
|----------|------|-----------|-------|
| $g_{Ca}$ | 1.0  | $\phi$    | 1/3   |
| $g_K$    | 2.0  | $I_{app}$ | 0.08  |
| $g_L$    | 0.5  | $V_1$     | -0.01 |
| $E_{Ca}$ | 1.0  | $V_2$     | 0.15  |
| $E_K$    | -0.7 | $V_3$     | 0.1   |
| $E_L$    | -0.5 | $V_4$     | 0.145 |

Table 1: The default parameters used for the ML model.

Now we describe the qualitative dynamics of the ML system using the  $V$ - $W$  phase-plane. We start by plotting the nullclines,  $\frac{dV}{dt} = 0$  and  $\frac{dW}{dt} = 0$ . The  $V$ -nullcline is  $W = (I_{ext} - I_{Ca} - I_L)/(g_K(V - E_K))$  and the  $W$ -nullcline is  $W = w_\infty(V)$ . Figure 2.1 is the phase portrait for the ML system. We see that there are three fixed points, which are located where the  $V$  and  $W$  nullclines intersect. Going from left to right along the  $V$  axis, the first fixed point is a stable node, the second is a saddle-point, and the third is an unstable spiral. “All” of the solutions for this parameter regime will converge to the stable node. However, the manner in which the solutions converge is based on what “side of the saddle node” they start on. If the initial conditions are set to the “right” of the stable manifold of the saddle-node (cyan curve in Figure 2.1), the solution is supra-threshold, whereas if the initial conditions are set to the “left” of the stable manifold, the solution is sub-threshold. The geometric differences between supra-threshold and sub-threshold can be seen in Figures 2.1 and 2.2.

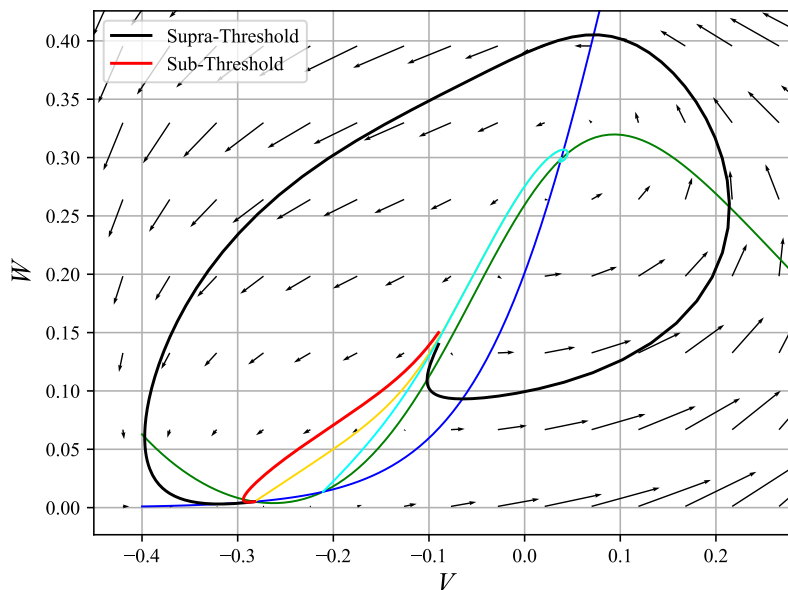


Figure 2.1: Showing the threshold dynamics in the phase plane.  $V$ -nullcline (green curve),  $W$ -nullcline (blue curve), supra-threshold (red curve), sub-threshold (black curve), stable manifold of the saddle-node (cyan curve), and a stable manifold of the stable node (yellow curve) in the phase plane.

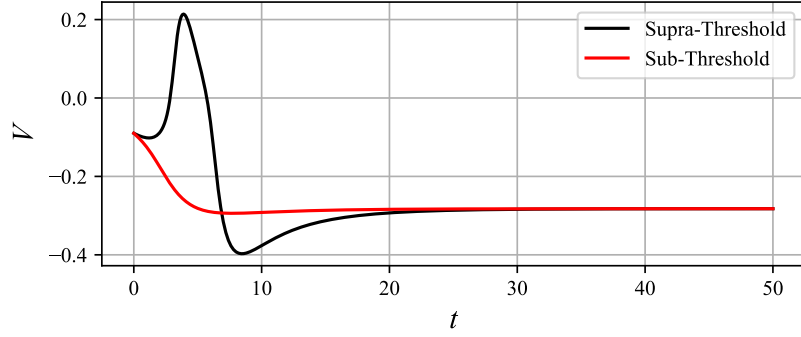


Figure 2.2: Showing the threshold dynamics plotting  $V$  against time, supra-threshold (red curve) and sub-threshold (black curve) in time.  $I_{ext} = 0.08$

In Figure 2.1, the supra-threshold solution (black curve) is “pulled” around by the unstable spiral; when the voltage is plotted against time in Figure 2.2, the solution exhibits a “spike” before converging to the steady state. On the other hand, the sub-threshold solution (red curve) does not go around the unstable spiral in Figure 2.1. Instead, it is quickly pulled into the stable node, and no spike occurs in Figure 2.2.

Note that there is a heteroclinic loop—a collection of trajectories that coalesce into an equilibrium point (Figure 2.3(a))—in the system. If the  $V$  nullcline is raised by increasing  $I_{ext}$ , a saddle-node bifurcation occurs, turning the heteroclinic loop into a homoclinic—a special case of a heteroclinic loop where the connection joins an invariant equilibrium (Figure 2.3(b)). Raising the nullcline any further, a stable limit cycle is born, putting the system into an oscillatory state shown in Figure 2.4 for  $I_{ext} = 0.1$ .

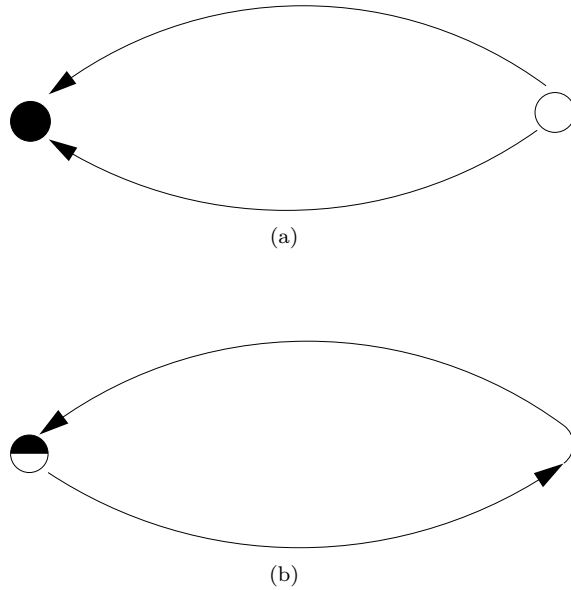
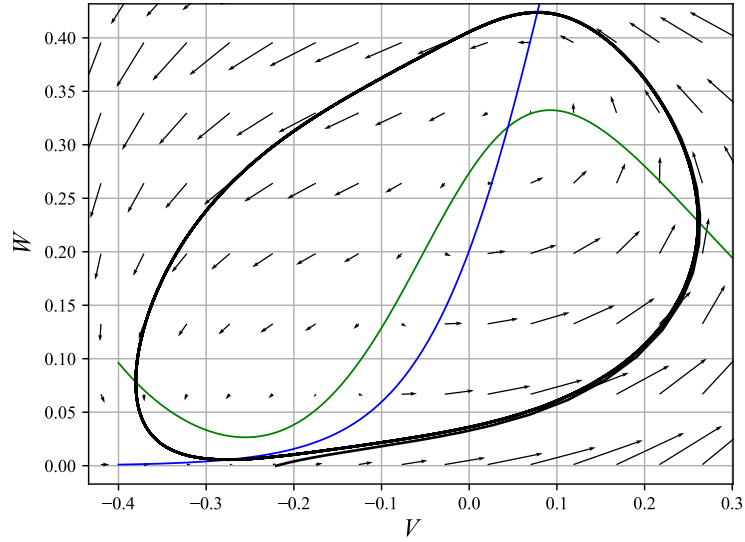
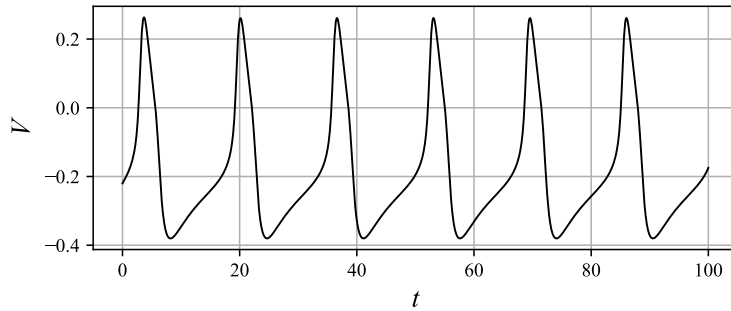


Figure 2.3: Depiction of (a) a heteroclinic loop, and a (b) homoclinic loop.



(a)



(b)

Figure 2.4: Setting  $I_{ext} = 0.1$  puts the system into an oscillatory state. (a) is the trajectory in the phase plane, showing the limit cycle, (b) is the time plot for the  $V(t)$  solution shown in (a).

To see when the onset of oscillations and other global changes occur, the bifurcation diagram is plotted varying the parameter  $I_{ext}$  in Figure 2.5. In Figure 2.5 there are two major bifurcations. The first is the saddle-node bifurcation (SNB), labeled  $LP_1$  that we expect from analyzing the phase-plane; along with the SNB comes a “saddle-node on an invariant cycle” (SNIC) bifurcation. The second bifurcation is a sub-critical Hopf bifurcation, labeled  $HB_1$ . In Figure 2.5, there is a branch of solutions that stems from  $HB_1$  comprised of the green and blue points. The green points are maximum and minimum values in  $V$  of stable limit cycles, whereas blue correspond to unstable limit cycles.

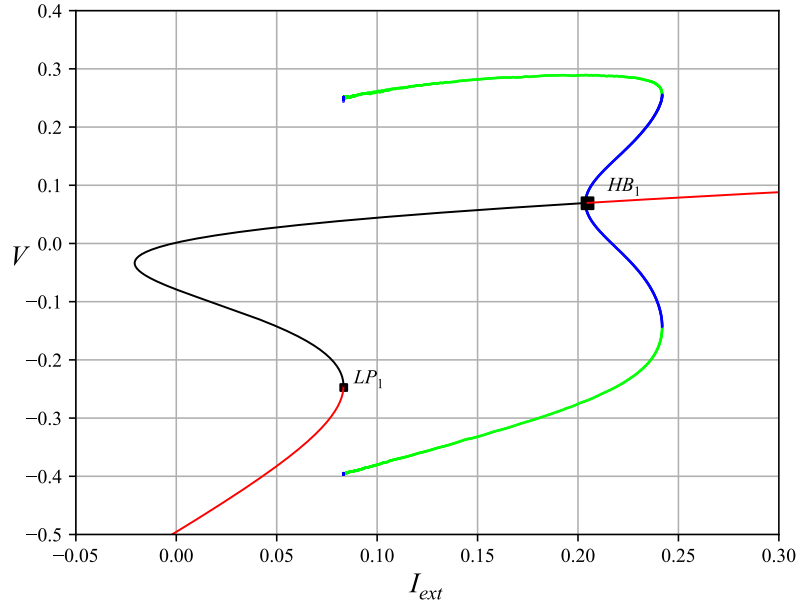


Figure 2.5: The bifurcation diagram for a single ML cell. Black curves represent unstable fixed points, red curves are stable fixed points, blue indicates the amplitudes of unstable limit cycles, and green are amplitudes of stable limit cycles. The points labeled  $LP_1$  and  $HB_2$  are respectively a saddle-node bifurcation and a sub-critical Hopf bifurcation. This bifurcation diagram was generated using XPPAUT [12].

### 3 Two Coupled Morris-Lecar Cells

#### 3.1 Adding “Diffusive” Coupling

We now consider two ML cells connected through diffusive coupling by applying Ohm’s law. The coupling conductance (referred to as the coupling strength) is represented by  $g_c$ . The equations governing the dynamics of two coupled cells are,

$$\begin{aligned} \frac{dv_1}{dt} &= f(v_1, w_1) + g_c(v_2 - v_1) \\ \frac{dw_1}{dt} &= \phi g(v_1, w_1) \\ \frac{dv_2}{dt} &= f(v_2, w_2) + g_c(v_1 - v_2) \\ \frac{dw_2}{dt} &= \phi g(v_2, w_2) \end{aligned}$$

where  $f$  is the reaction function in equation (2.1) and  $g$  is the function in the recovery equation (2.2). Figure 3.1 is a depiction showing that the two cells can be thought of as two coupled oscillators connected by a resistor. The coupling is only through fast variables,  $v_1$  and  $v_2$ , because physiologically, electrically coupled cells only communicate via the membrane potential.

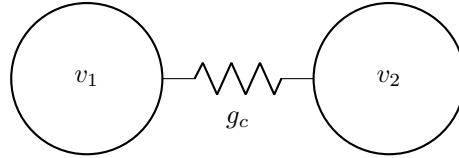


Figure 3.1: A depiction of two oscillators connected by a resistor.

### 3.2 What is Diffusive Coupling Doing

The expected behavior of two diffusively coupled cells is that they eventually converge to a synchronous state. When  $v_1 > v_2$  the coupling term will cause  $v_2$  to increase in order to “catch up” to  $v_1$ , and when  $v_1 < v_2$  it will give  $v_1$  a “boost” and  $v_2$  will be “pulled down” by  $v_1$  because  $g_c(v_1 - v_2) < 0$ . Figure 3.2(a) illustrates the effect of diffusive coupling. The  $v_1$  (black curve) has supra-threshold initial conditions and  $v_2$  has sub-threshold initial conditions.  $v_1$  elicits a spike, and because of the coupling, the  $v_2$  is “pulled” up by  $v_1$ , causing a delayed spike. However,  $v_2$  does not always get pulled into a supra-threshold state. Figure 3.2(b) shows that when the initial voltage for  $v_2$  is started far below the steady state,  $v_2$  does not spike.

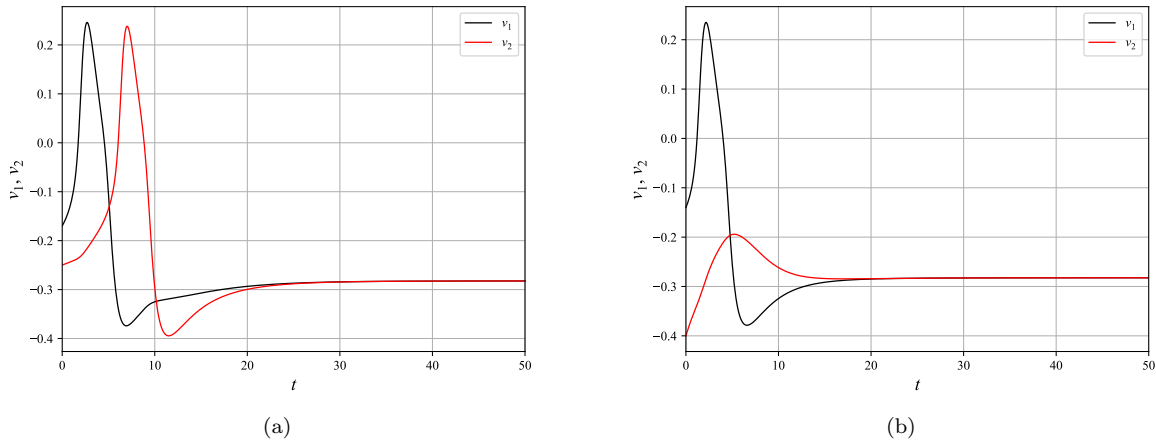


Figure 3.2: Two numerically simulated solutions in a non-oscillatory state with (a) the second cell is pulled up by the first causing a delayed spike, (b) the initial voltage for the second cell is too low for it to enter a supra-threshold state.  $g_c = 0.1$

Figure 3.3 shows when the system is in an oscillatory state ( $I_{ext} = 0.1$ ). The two solutions begin in an asynchronous state, but quickly lock phase as the diffusive coupling brings them together.

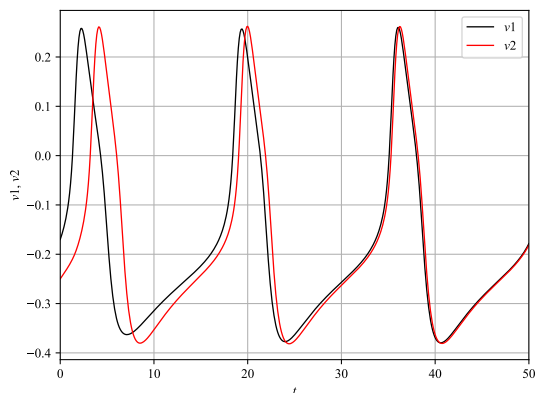


Figure 3.3: A numerically simulated solution in an oscillatory state. The two oscillating cells converge to phase lock.  $I_{ext} = 0.1$ ,  $g_c = 0.1$

### 3.3 Echo Waves in Two Diffusively Coupled Cells

Figure 3.2 shows that the solutions depend on the initial conditions. Because of the different solutions obtained in Figures 3.2 (a) and (b), there must be a point where the solution for  $v_2$  transitions from sub-threshold to supra-threshold. The question is: What types of behavior will the system elicit when the initial conditions are set closely to the transition point? Fixing the initial conditions for  $v_1$ ,  $w_1$ , and  $w_2$ , Figure 3.4 shows how changing the initial condition for  $v_2$  such that it is closer to the threshold limit that would result in a solution similar to Figure 3.2(b).

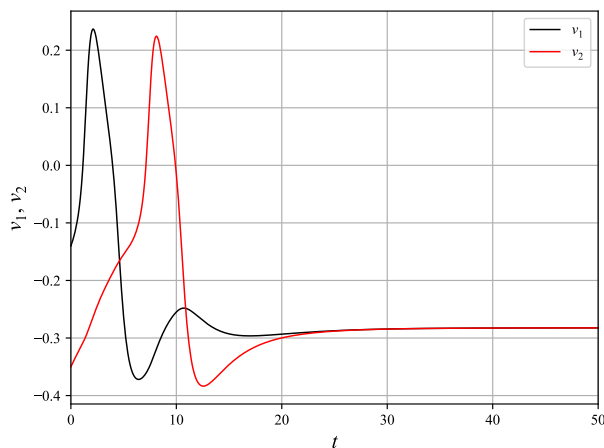


Figure 3.4: The solution curve after changing the initial conditions, highlighting the “blip” we were seeing from  $v_1$ .  $g_c = 0.1$

In Figure 3.4, during the refractory period—period of less excitability immediately following the action potential (spike)—of  $v_1$  a “blip” in the solution occurs. This blip raises the question of whether or not  $v_1$  can be re-excited, causing an “echo wave” or “reflection”. An echo wave is an additional spike in the leading cell—the cell that exhibits the first spike—caused by a coordinated delay in the spike of the following cell—the cell that spikes after the leading cell due to the coupling dynamics. Systematically changing the initial conditions for  $v_2$  leads to an echo wave which is seen in Figure 3.5.

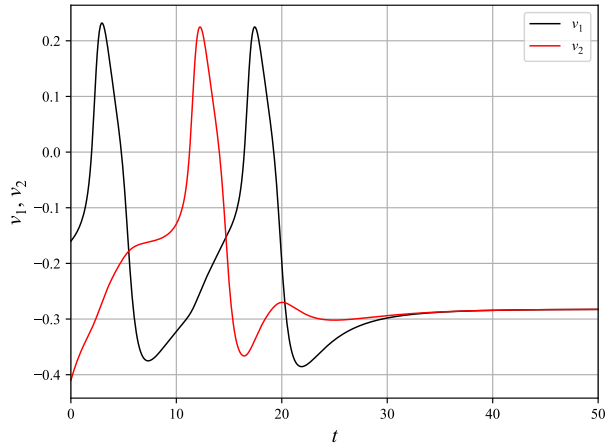


Figure 3.5: The solution curve after changing the initial conditions more in order to cause an echo wave for  $v_1$ .  $g_c = 0.1$

Note that a blip now occurs in  $v_2$ 's refractory period. Further changing the initial conditions for  $v_2$  (getting closer to the transition point) leads to a second echo wave, this time in  $v_2$ . Figure 3.6 shows the second echo wave and how  $v_1$  is now eliciting signs of yet another echo wave. In fact, the more  $v_2(t_0)$  is varied, the more echo waves appear (see Figure 3.7).

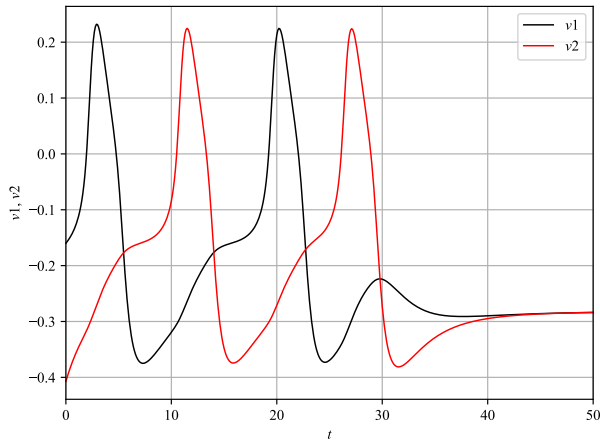


Figure 3.6: Results of varying initial conditions again for  $v_2$ , causing an echo wave for both  $v_1$  and  $v_2$ .  $g_c = 0.1$

The initial condition for  $v_2$  is systematically varied (using Algorithm 1 in section 6 Appendix). The algorithm mimics a continuous increase in  $v_2(t_0)$  by simulating all achievable numbers of echo waves for a given level of precision by starting from an initial condition that leads to a solution similar to Figure 3.2(b) (this initial condition is referred to as the min) and ending at an initial condition  $v_2(t_0) = v_1(t_0)$  (referred to as the max). Using the algorithm, more echo waves are found as  $v_2(t_0)$  is “fine-tuned.” As the initial condition for  $v_2$  is slowly increased, the increase in echo waves (Figure 3.7) is seen.

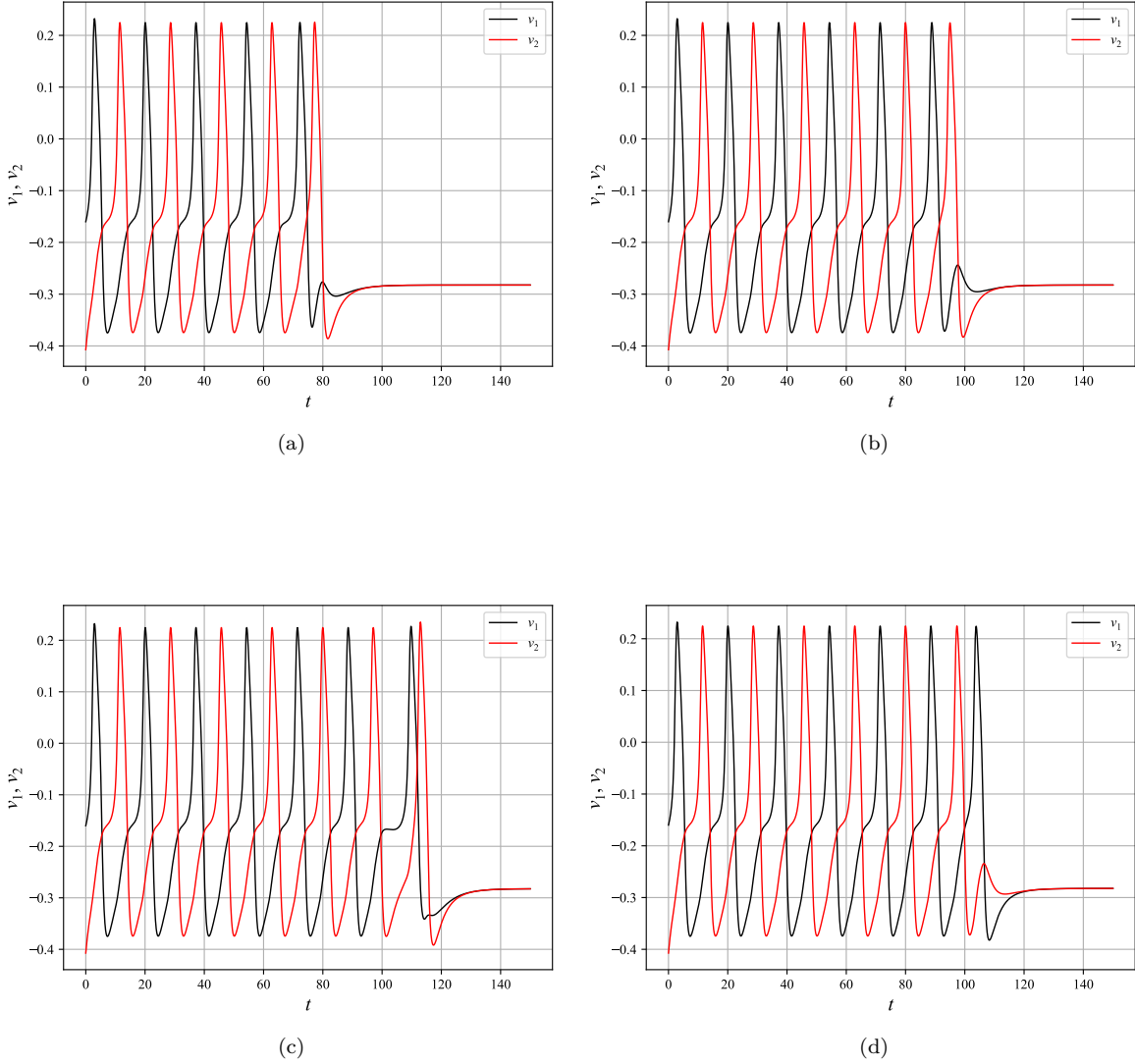


Figure 3.7: Simulated solutions after using Algorithm 1 in section 6 to various degrees of precision. (a) step size  $10^{-11}$  can find 5 total spikes for both trajectories, (b) step size  $10^{-14}$  can find 6 total spikes for both trajectories, (c) step size  $10^{-16}$  can find 7 total spikes for both trajectories, (d) step size  $10^{-15}$  can find 7 spikes in  $v_1$  and 6 in  $v_2$ .  $g_c = 0.1$

With the results generated by the algorithm in Figure 3.7, a pattern sequence in which the number of echo waves that occur is seen. We can define the notation  $N : M$  to represent the pattern seen in the simulated solutions, where  $N$  is the number of spikes in  $v_1$  and  $M$  is the number of spikes in  $v_2$ . Figure 3.2(a) is a  $1 : 1$ , 3.2(b) is a  $1 : 0$ , and Figure 3.6 is a  $2 : 2$ . If  $v_2(t_0)$  were to change in a continuous fashion so that the system changed from a  $1 : 1$  pattern to a  $1 : 0$  pattern, the sequence of observed patterns would be:

$$1 : 1, 2 : 2, 3 : 3, \dots, N : N, \dots, \dots, N + 1 : N, \dots, 3 : 2, 2 : 1, 1 : 0 \quad (3.1)$$

As more echo waves happen,  $v_2(t_0)$  is approaching an undetermined value that we denote as  $v_2^*$ , and the number of echo waves becomes increasingly sensitive to the initial condition of  $v_2$ . That is, the level

of precision required to generate any  $N : N$  pattern becomes infinitesimally small as  $N$  increases. If the initial condition were set at  $v_2^*$ , an infinite number of echo waves would occur. This indicates that the initial conditions are getting closer to the stable manifold of an unstable limit cycle of an anti-phase solution. Figure 3.8 shows a schematic of for the three cases:  $v_2(t_0) < v_2^*$ ,  $v_2(t_0) = v_2^*$ , and  $v_2(t_0) > v_2^*$ .  $v_2^*$  lies on a stable manifold (blue-gray surface in Figure 3.8) of an unstable limit cycle. As the  $v_2(t_0)$  goes from being less than  $v_2^*$  to greater, the “side” of the manifold the trajectory is on is different. If  $v_2(t_0) > v_2^*$  (Figure 3.8(c)) an  $N : N$  pattern will be seen, whereas if  $v_2(t_0) < v_2^*$  (Figure 3.8(a)) an  $N : N - 1$  will occur. However, Figure 3.8(b) depicts when  $v_2(t_0) = v_2^*$ . The trajectory falls exactly on the stable manifold and follows the unstable limit cycle indefinitely. An outline of the unstable limit cycle is seen in Figure 3.9.

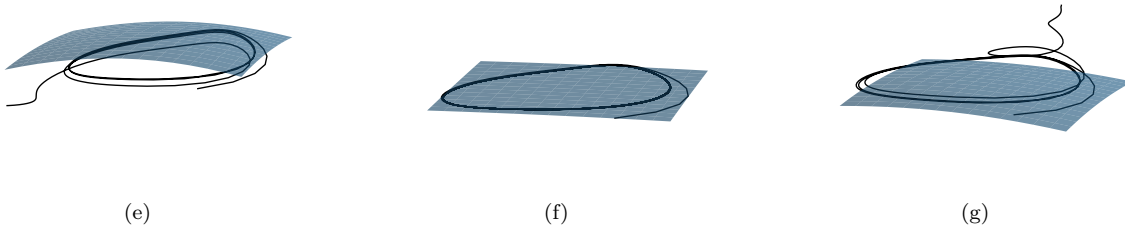


Figure 3.8: Visualization of changing  $v_2(t_0)$  from (a)  $v_2(t_0) < v_2^*$ , (b)  $v_2(t_0) = v_2^*$ , and (c)  $v_2(t_0) > v_2^*$ .

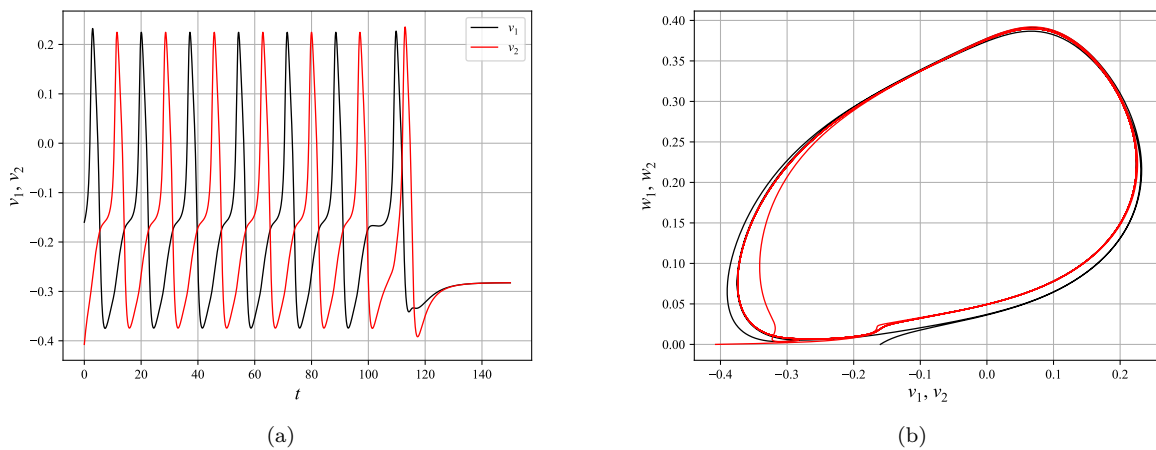


Figure 3.9: Plotting a  $7 : 7$  pattern in phase space in order to see the unstable limit cycle.  $g_c = 0.1$

### 3.4 Quantitative Bifurcation Analysis of Two Diffusively Coupled Cells

The evidence of an unstable limit cycles and their association with echo waves leads us to dig deeper to see if and when an unstable anti-phase limit cycle exists when the cells are excitable (i.e. not self-oscillatory), and to see what other behaviors can be uncovered. Figure 3.10 shows the bifurcation diagram for the two coupled cells studied in section 3.3.

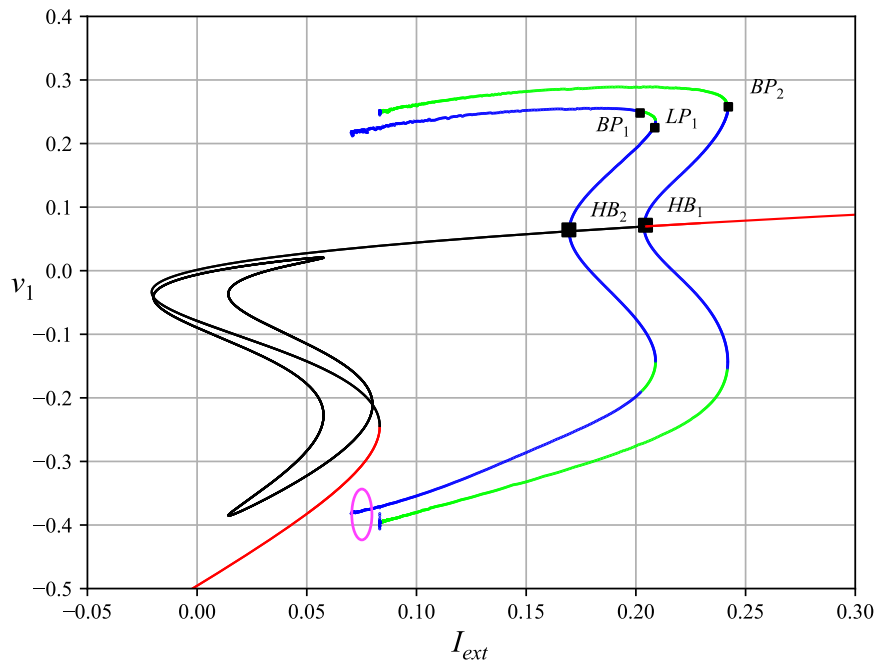


Figure 3.10: The bifurcation diagram for two coupled cells,  $g_c = 0.1$ . This bifurcation diagram was generated using XPPAUT [12].

Comparing this bifurcation diagram to the bifurcation diagram for a single cell (Figure 2.5), there is striking similarity: the steady-states, limit-cycles, and the saddle-node and SNIC bifurcations that were present for the single cell appear on the bifurcation diagram for coupled cells. These correspond to synchronous activity in the coupled cells. Note, however, there are also asynchronous steady states and limit cycles indicated on the two cell bifurcation diagram. In particular, in the region of parameter space that we observed echo waves, there do indeed exist unstable anti-phase limit cycles and the cells are excitable. This region is indicated on Figure 3.10, by a pink ellipse marked near the minimum  $v_1$  of limit cycles. Initial conditions taken near the unstable limit cycles in this region result in solutions similar to the one seen in Figure 3.11(d).

### 3.4.1 Following the Branch of Asynchronous Solutions

One notable difference between the bifurcation diagrams for a single cell and two coupled cells is the existence of a second Hopf bifurcation (labeled  $HB_2$  in Figure 3.10). The solutions that lay on the solution branches associated with this new bifurcation point are asynchronous, i.e., the activity of the two cells are out of phase with one another. As one follows the branch, several behaviors are seen. Solutions exhibiting: (I) unstable quasiperiodicity (Figure 3.11(a) blue points between  $HB_1$  and the bifurcation point labeled  $LP_1$  in Figure 3.10); (II) stable anti-phase (Figure 3.11(b) green points between bifurcation points labeled  $LP_1$  and  $BP_1$  in Figure 3.10); (III) unstable anti-phase (Figure 3.11(c) seen converging to a synchronous solution), until the end of the branch where the SNIC bifurcation occurs.

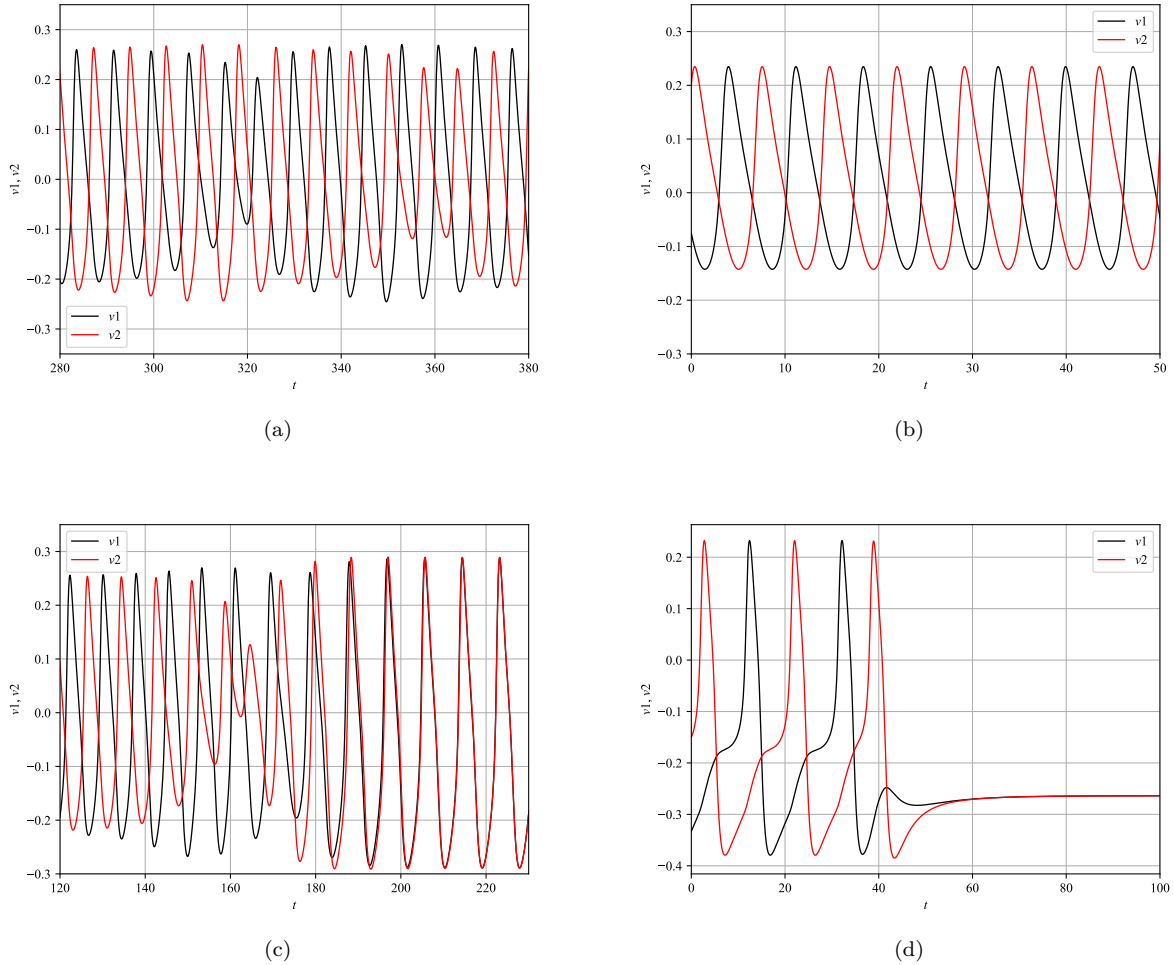


Figure 3.11: Behaviors seen along branch of solutions associated with  $HB_2$ : (a) quasiperiodic solution that can be found between bifurcation points  $HB_2$  and  $LP_1$  in Figure 3.10, (b) stable anti-phase solution that can be found between bifurcation points  $LP_1$  and  $BP_1$  in Figure 3.10, (c) anti-phase that is seen converging to a synchronous solution which can be found between the bifurcation point  $BP_1$  and the SNIC bifurcation in Figure 3.10, (d) exhibiting echo waves associated with unstable limit cycles in parameter space near the pink ellipse in Figure 3.10.  $g_c = 0.1$

### 3.4.2 Varying the Coupling Strength Between Cells

If the coupling strength between two cells were to be increased, each cell would have more influence on the other. One would expect that (due to the extra influence) the two cells would “want” to be in a synchronous state. However, this is not necessarily the case. In Figure 3.12(b), the parameter region of  $I_{ext}$  where echo waves exist is much larger when the coupling strength is increased, compared to Figure 3.12(a) where the coupling strength is decreased.

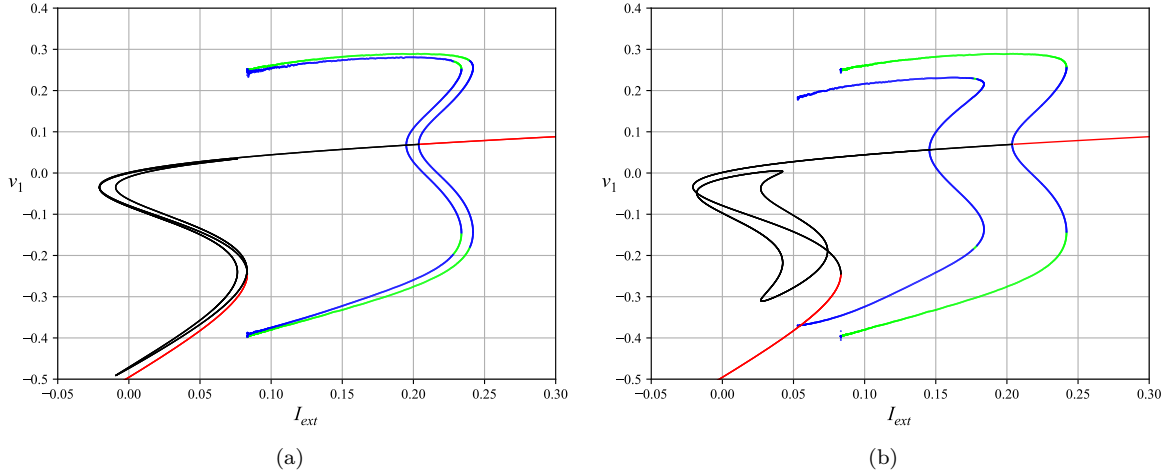


Figure 3.12: Bifurcation diagrams with varying values for  $g_c$ , (a)  $g_c = 0.025$ , (b)  $g_c = 0.175$ . These bifurcation diagrams were generated using XPPAUT [12].

## 4 Reaction Diffusion System Using the Morris-Lecar Model

### 4.1 Diffusion

Electrochemical waves of excitation propagate through heart tissue in order to cause a coordinated mechanical contraction. Reaction-diffusion equations have been used to model these electrochemical waves [7, 8, 9]. Adding spatial diffusion of voltage  $V$  to the ML model gives the reaction-diffusion system,

$$\frac{\partial V}{\partial t} = D \frac{\partial^2 V}{\partial x^2} + f(V, W) \quad (4.1)$$

$$\frac{\partial W}{\partial t} = \phi g(v_1, w_1) \quad (4.2)$$

The diffusion term  $D \frac{\partial^2 V}{\partial x^2}$  is proportional to the curvature of  $V(t, x)$  in space,  $x$ . This implies that whenever  $V(t, x)$  has negative curvature at  $x$  ( $\frac{\partial^2 V}{\partial x^2} < 0$ ), diffusion will act to decrease  $V(t, x)$  in time, and the more negative  $\frac{\partial^2 V}{\partial x^2}$  is, the faster  $V$  will decrease. If the curvature is positive, we have the opposite effect. Over time, this process acts to smooth  $V(t, x)$  over the domain. To illustrate these effects of diffusion, we simulate the diffusive equation,  $\frac{\partial V}{\partial t} = D \frac{\partial^2 V}{\partial x^2}$ , i.e., equation (4.1) without the reaction term. As can be seen in Figure 4.1, the areas of high curvature—in the center of the domain of Figure 4.1(a)—change at a much faster rate in the direction of their concavity than those with little to no curvature—the endpoints of each plot in Figure 4.1.

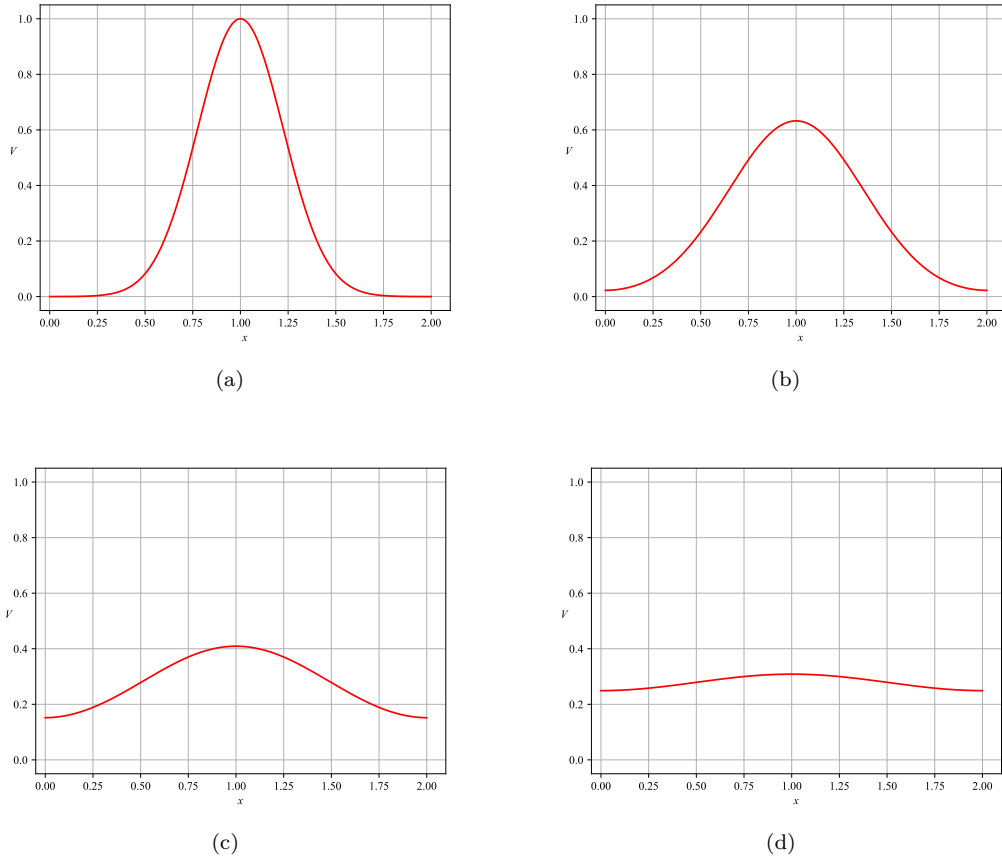


Figure 4.1: Snapshots of one-dimensional diffusion over time across the spacial domain  $[0, 2]$ , (a)  $t = 0$ , (b)  $t = 15$ , (c)  $t = 50$ , (d)  $t = 100$ .

## 4.2 Numerical Methods: Discretization of Differential Equations

Analytical solutions to the ML system (e.g. (4.1) and (4.2)) do not exist, therefore we discretize it (see Figure 4.2) and solve it numerically. Discretizing the diffusion process is equivalent to coupling “cells” via a resistor.



Figure 4.2: Representation for a discretized one-dimensional piece of cardiac tissue where each cell is coupled via a resistor with resistance  $\sigma$ .

Using the Crank-Nicolson method (which includes the second-order centered finite difference formula) we discretize equation (4.1) into,

$$\frac{V_i^{n+1} - V_i^n}{\Delta t} = \frac{D}{2\Delta x^2} ((V_{i+1}^{n+1} - 2V_i^{n+1} + V_{i-1}^{n+1}) + (V_{i+1}^n - 2V_i^n + V_{i-1}^n)) + f_{RK}(V_i^n, W_i^n) \quad (4.3)$$

where  $f_{RK}(V_i^n, W_i^n)$  is the explicit fourth-order Runge-Kutta method such that,

$$\begin{aligned}
K_1 &= \Delta t F(t_n, Y_i^n) \\
K_2 &= \Delta t F\left(t_n + \frac{\Delta t}{2}, Y_i^n + \frac{K_1}{2}\right) \\
K_3 &= \Delta t F\left(t_n + \frac{\Delta t}{2}, Y_i^n + \frac{K_2}{2}\right) \\
K_4 &= \Delta t F(t_n + \Delta t, Y_i^n + K_3) \\
Y_i^{n+1} &= Y_i^n + \frac{1}{6}(K_1 + 2K_2 + 2K_3 + K_4)
\end{aligned}$$

where  $F$  is the vector of functions (2.1) and (2.2),  $Y_i^n = \begin{pmatrix} V_i^n \\ W_i^n \end{pmatrix}$ , and  $K_i$  are vectors. The system is now in an implicit-explicit form where the implicit Crank-Nicolson scheme is used for the diffusion component, and the explicit fourth-order Runge-Kutta is used for the non-linear component. Letting  $\sigma = D \frac{\Delta t}{2\Delta x^2}$  and rearranging (4.3) we get,

$$-\sigma V_{i+1}^{n+1} + (1 + 2\sigma)V_i^{n+1} - \sigma V_{i-1}^{n+1} = \sigma V_{i+1}^n + (1 - 2\sigma)V_i^n + \sigma V_{i-1}^n + \Delta t f_{RK}(V_i^n, W_i^n) \quad (4.4)$$

With this form, a linear system of  $A\tilde{V}^{n+1} = B\tilde{V}^n + \Delta t\tilde{f}^n$  can be used to numerically solve the system with no-flux boundary conditions such that,

$$A = \begin{pmatrix} 1+\sigma & -\sigma & & & \\ -\sigma & 1+2\sigma & -\sigma & & \\ & \ddots & \ddots & \ddots & \\ & & -\sigma & 1+2\sigma & -\sigma \\ & & & -\sigma & 1+\sigma \end{pmatrix}, \quad B = \begin{pmatrix} 1-\sigma & \sigma & & & \\ \sigma & 1-2\sigma & \sigma & & \\ & \ddots & \ddots & \ddots & \\ & & \sigma & 1-2\sigma & \sigma \\ & & & \sigma & 1-\sigma \end{pmatrix}$$

$$\tilde{V}^{n+1} = \begin{pmatrix} V_0^{n+1} \\ \vdots \\ V_N^{n+1} \end{pmatrix}, \quad \tilde{V}^n = \begin{pmatrix} V_0^n \\ \vdots \\ V_N^n \end{pmatrix}, \quad \tilde{f}^n = \begin{pmatrix} f(V_0^n, W_0^n) \\ \vdots \\ f(V_N^n, W_N^n) \end{pmatrix}$$

Because the system is tridiagonal, each time-step can be solved in  $O(n)$  time which becomes useful when making the domain larger and using finer step sizes. The parameters used are:  $\Delta x = 0.001$ ,  $\Delta t = 0.03$ , and  $D = 0.001$ .

### 4.3 Traveling Waves in a 1D Domain

In our spatially extended ML system, an adequate stimulus will initialize an action potential similar to one seen in Figure 2.1(b). However, because we are now working in space with diffusive coupling, the system develops a traveling wave along our one dimensional domain.

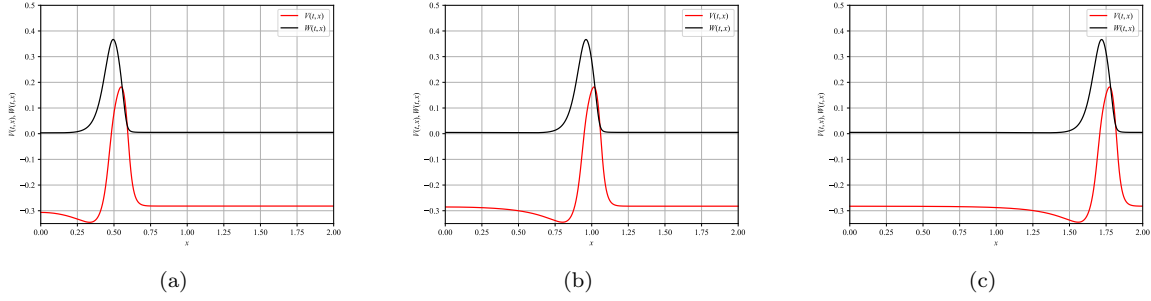


Figure 4.3: A wave travelling along our simulated rod across our domain, Where the red curve is  $V(t, x)$  and the black curve is  $W(t, x)$ .

Figure 4.3 shows how an action potential travels along the one-dimensional domain. As the wave moves in the  $+x$ -direction, the tissue is depolarized by the wavefront and is eventually “excited”. The diffusive coupling allows the action potential to spread but the excitatory dynamics keep it afloat. Figure 4.4 shows a space-time plot of the wave in Figure 4.3 traveling across the entire domain. A space-time plot shows how an action potential travels across a domain over time. The blue represents the non-excited media while the green and orange shows the excitation traveling as time progresses.

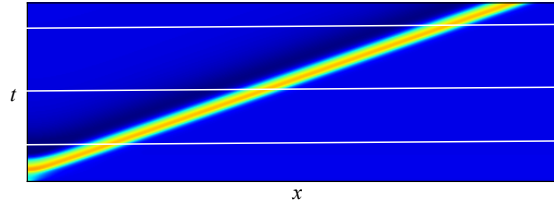


Figure 4.4: Space-time plot to show wave propagating in space through time first shown in Figure 4.3. The white lines are the times of the snapshots used for the plots in Figure 4.3.

#### 4.4 Reflections on a 1D Domain

The lumped coupling conductance used in our two “cell” model (section 3) is analogous to adding a non-excitable region into the domain. The question is then asked: What behaviors will be seen when this non-excitable “gap” is added, and can this gap lead to echo wave like behavior similar to what was seen in Figures 3.2 - 3.9? In order to simulate the heterogeneity, a slight modification is made to the equations (4.1) and (4.2). Our new system is defined as,

$$\frac{\partial V}{\partial t} = D \frac{\partial^2 V}{\partial x^2} + S(x)f(V, W) \quad (4.5)$$

$$\frac{\partial W}{\partial t} = S(x)\phi g(V, W) \quad (4.6)$$

where,

$$S(x) = \begin{cases} \delta & x \in [X_l, X_r] \\ 1 & \text{otherwise} \end{cases} \quad (4.7)$$

$S(x)$  is a function to represent a sudden decrease in the excitability of the media, and the left and right endpoints of our heterogeneity are  $X_l$  and  $X_r$ . We let  $\delta$  be zero, which means dynamics in the gap are purely diffusive.

Figure 4.5 shows an example of a simulation with small gap length  $L = 0.04$ . The wave travels across the proximal side of the gap and experiences a minor delay when reaching the gap. The delay is brief, and the wave quickly returns to its fully excited state and continues to propagate through the remainder of the domain. Figure 4.6 illustrates the case of a large gap length  $L = 0.06$ . The wave now cannot source enough current through the gap to excite the distal side of the gap. This causes the wave to be blocked and not propagate through the remainder of the domain.

Because of the similarities between the gap model and the two “cell” model, the parameter region for  $L$  between these two cases (pass and block) is looked into and the gap length is set to  $L = 0.052$ .  $L = 0.052$  leads to a new behavior as shown in Figure 4.7. The wave successfully crosses the gap like it did in figure 4.5, however because the delay going through the gap was long, the tissue on the proximal side was able to recover enough to be excited again. Because of this, the re-excitation on the proximal side causes an echo or “reflected” wave to propagate in the rearward (relative to the original wave) direction.

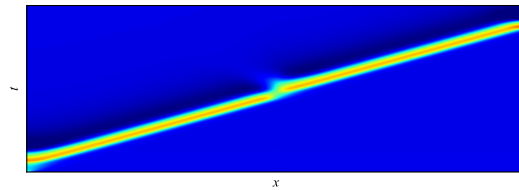


Figure 4.5: Results after setting  $L = 0.04$ , where only a brief interruption occurs in the wave because of the gap.

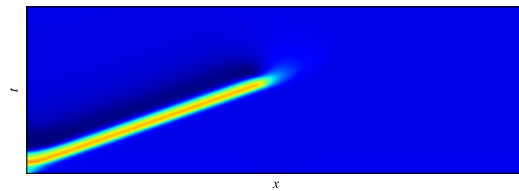


Figure 4.6: Results after setting  $L = 0.06$ , where the distal side of the gap does not become excited.

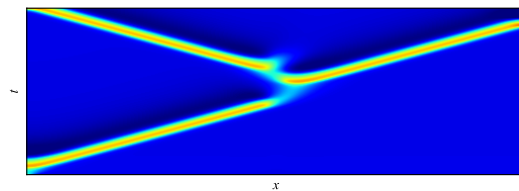


Figure 4.7: Results after setting  $L = 0.052$ , where the delay is long enough to produce a reflected wave.

For gap length  $L = 0.05$ , a second reflected wave is created from the first reflection (Figure 4.8(a)). As  $L$  “refined” more and more to a certain value we call  $L^*$ —more of these reflections occur. We see this behavior illustrated in the results shown in Figure 4.8. This is the same phenomenon as in section 3.3, thus the same notation can be used and we define an  $N : M$  reflection pattern to represent activity in which  $N$  waves occur on the proximal side of the gap (including the original), and  $M$  waves occur on the opposing or distal side of the gap. The results in Figures 4.5-4.8 suggest that if  $L$  is increased in a continuous manner from the wave being able to quickly “pass” the gap (Figure 4.5) to the gap blocking the wave (Figure 4.6),

the following sequence would occur:

$$1 : 1, 2 : 2, 3 : 3, \dots, N : N, \dots, \dots, N + 1 : N, \dots, 3 : 2, 2 : 1, 1 : 0. \quad (4.8)$$

This same sequence has been observed in [4, 10]. As more and more reflections occur, we approach the critical value  $L^*$ . The resulting patterns suggests that there exists a stable manifold of an unstable limit cycle. If the gap length was set to exactly  $L^*$ , we would land on this manifold and would generate an infinite number of reflections. Figure 4.8 shows how solutions exhibit more reflections the closer  $L$  is to  $L^*$ .

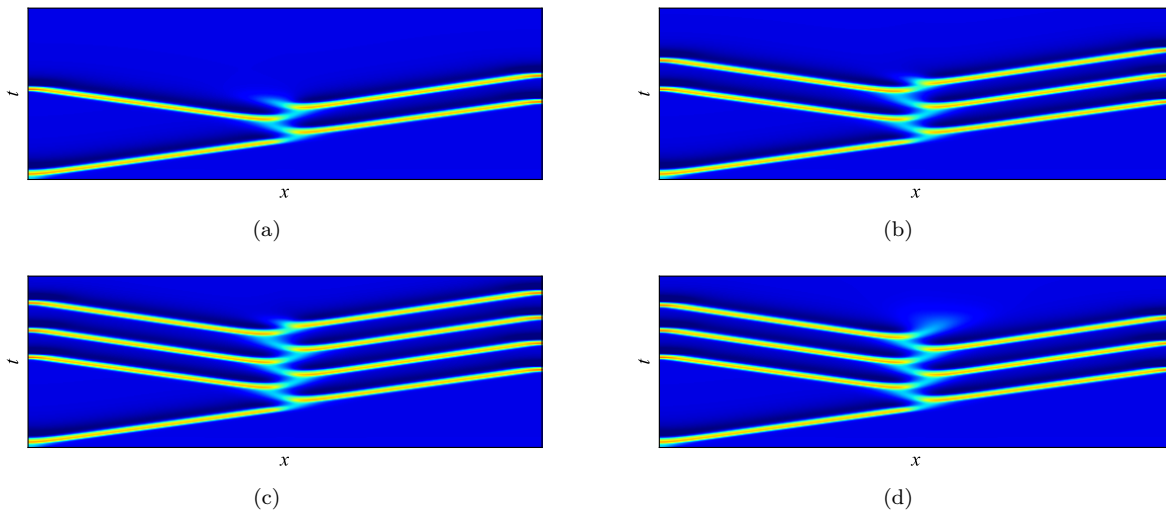


Figure 4.8: Results of varying the size of  $L$  in order to get more reflections, where (a) is a 2;2, (b) is a 3;3, (c) is a 4;4, and (d) is a 4;3.

## 4.5 Experimenting With Two Gaps in a 1D Domain

Figure 4.9 shows the result of adding a second gap into the domain. With the introduction of the second gap, finding a solution with an infinite number of reflections now becomes easier. In Figure 4.9, two gaps of size  $L = 0.052$  are placed at the one-third and two-thirds mark in the domain. Note that for a single gap,  $L = 0.052$  results in a 2 : 1 pattern, so only a single reflection happens. However, because of the second gap, the reflected wave from the rightmost gap reflects a wave causing the cycle to repeat indefinitely.

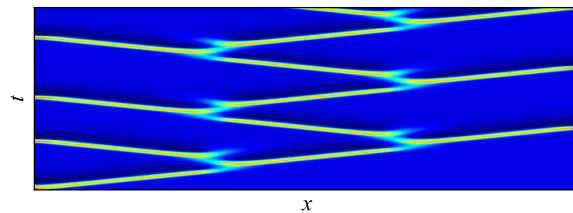


Figure 4.9: Numerical simulation using two equally sized gaps in the domain of gap size  $L = 0.052$ .

## 4.6 Extending to a 2D Spatial Domain

Adding a second spatial dimension allows the wave to propagate in two directions. Extending to a two-dimensional model is essential because it allows us to simulate much more realistic conditions of an electrochemical wave traveling across the surface of cardiac tissue, and now there are many more scenarios

when simulating the heterogeneity as there are more possibilities for size, shape, and area of the inexcitable region. The reaction diffusion equations for two dimensions are now,

$$\frac{\partial V}{\partial t} = D \left( \frac{\partial^2 V}{\partial x^2} + \frac{\partial^2 V}{\partial y^2} \right) + f(V, W) \quad (4.9)$$

$$\frac{\partial W}{\partial t} = \phi g(V, W) \quad (4.10)$$

Figure 4.10 shows, much like in section 4.2, when our, now two dimensional, domain is discretized, it can be thought of as a finite number of discretized, one-dimensional domains “stacked” and connected to each other. Now each cell is being influenced by four other cells, two in the  $x$ -direction and two in the  $y$ -direction. This makes implementing numerical solver more tedious, but the underlying dynamics for the reaction-diffusion system remain the same. To run the simulations, we use the alternating direction implicit (ADI) method with the same Crank-Nicolson scheme used in section 4.2. The domain being used to represent our medium is referred to as the set  $T \subset \mathbb{R}^2$ , where  $T = \{0, \Delta x, \dots, N\Delta x\} \times \{0, \Delta y, \dots, M\Delta y\}$ , and  $\Delta x = \Delta y$ ,  $N = M$ . In this section  $\Delta x = \Delta y = 0.01$  and  $N = M = 200$  unless otherwise stated.

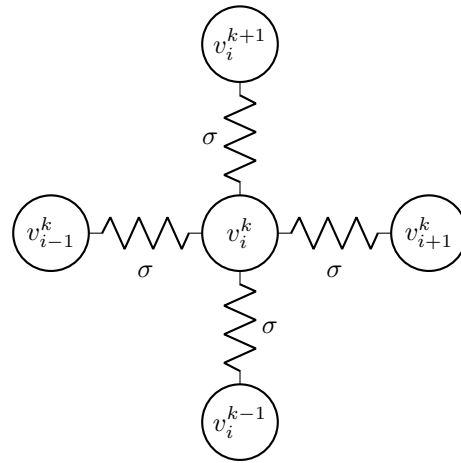


Figure 4.10: A depiction of how the cells in the grid are connected at some  $(x_i, y_k) \in T$ .

## 4.7 Traveling Waves in a 2D Domain

To initiate an essentially one-dimensional wave in our two-dimensional system, the initial conditions for  $V(t_0, x_i, y_k)$  are set to be a square wave that uniformly spans the  $x$ -direction, i.e.,  $V(t_0, x_i, y_k) = 1$  if  $0 \leq y_k \leq 0.05$  otherwise  $-0.28$ , where  $-0.28$  is approximately the steady state.  $W(t_0, x_i, y_k) = 0$  for each  $(x_i, y_k)$  in the domain. Figure 4.11 shows how the wave travels over time. As this wave travels across the domain, it travels in exactly the same manner as previously seen in Figure 4.3. Moreover, if a cross section was taken we would see the same space-time plot seen in Figure 4.4.

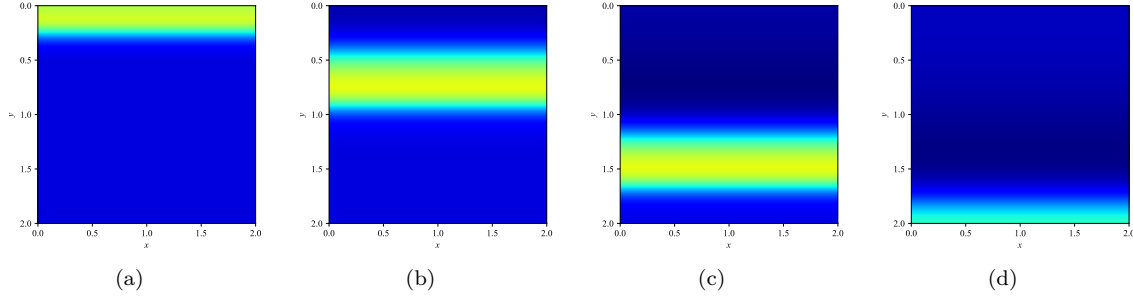


Figure 4.11: Square wave travelling across the domain in the  $y$ -direction.

## 4.8 Reflections on a 2D Domain

Now that the system has two spatial dimensions, we model the gap as a two-dimensional localized region contained within the domain. We define  $I \subseteq T$  to be the region of non-excitable media, where we take  $I$  to be several shapes. For example, if  $I$  were to be an ellipse with major and minor axes of size  $a$  and  $b$  centered in  $T$ ,  $I$  would be defined,

$$I = \left\{ (x_i, y_k) \in T : \frac{(x_i - \frac{\Delta x}{2}N)^2}{a^2} + \frac{(y_k - \frac{\Delta y}{2}M)^2}{b^2} \leq 1 \right\}$$

For this model,  $V$ ,  $W$ , and  $S$  are now function of both  $x$  and  $y$ .

$$\frac{\partial V}{\partial t} = D\nabla^2 V + S(x, y)f(V, W) \quad (4.11)$$

$$\frac{\partial W}{\partial t} = S(x, y)\phi g(v_1, w_1) \quad (4.12)$$

where,

$$S(x, y) = \begin{cases} \delta & (x, y) \in I \\ 1 & \text{otherwise} \end{cases} \quad (4.13)$$

During ischemic infarction, the spatial distribution of myocyte death spreads as a wavefront moving in the radial direction[1]. This means that the “patch” of ischemic tissue will spread in a diffusive process and the region in which the tissue lives will have a smooth boundary. To emulate the smoothness,  $I$  is set to be an ellipse, and to study the irregular shapes that myocardial ischemia can have, multiple ellipses are used.

Similarly to having a small gap in a one-dimensional domain, Figure 4.12 shows an example of when a small, non-excitable ( $\delta = 0$ ) ellipse ( $a = 0.08$ ,  $b = 0.45$ ) is placed in the center of a two-dimensional domain, the wave will experience a brief delay when traveling through the heterogeneity. After reaching the end of the non-excitable region, the wave returns back to its original, fully excited state. Figure 4.13 illustrates what happens when the axes length of the ellipse is increased in the  $y$ -direction ( $a = 0.4$ ,  $b = 0.8$ ). The center of the wave now experiences a large delay that stops it once it has entered the inexcitable region. However, because there is room on the sides of the inexcitable region, the wave can continue and “go around” the inexcitable region. Both of these cases are considered the same and are referred to as a “pass.” Figure 4.14 shows a case when the size of the heterogeneity is increased more ( $a = 0.21$ ,  $b = 0.97$ ). The entire wave is delayed when it reaches the heterogeneity, causing the wave to go below the excitation threshold, preventing the wave from reaching the distal side of the heterogeneity. This is referred to as a “block.”

In Figure 4.12(c), we see the wave diffusing into the inexcitable region, but the region is too large for the wave to reach the proximal side of the heterogeneity. Decreasing the size of the minor axis will allow the wave to be delayed the right amount of time in order for it to fully propagate through the non-excitable region while also having the media on the proximal side be recovered enough to take another action potential. This means the current that diffuses into the heterogeneity can re-excite the proximal side. Increasing the

size of the major axis delays the reflected wave, allowing the media on the distal side to be recovered by the time the wave reaches the distal side. When the wave has returned to the center of the distal side, the proximal side is now recovered again and the residual current in the non-excitable region causes another reflected wave to happen, then the cycle continues indefinitely, and two spiral waves are formed. Figure 4.15 illustrates this process.

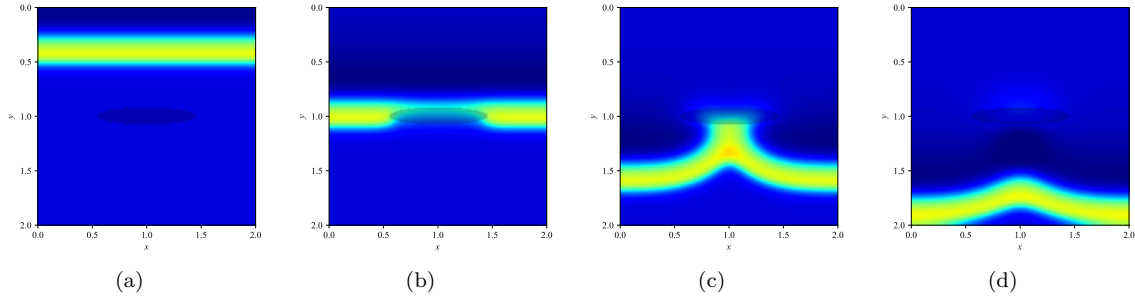


Figure 4.12: Snapshots of a wave passing through a small ischemic region. Minor axis length,  $a = 0.08$ , major axis length,  $b = 0.45$ .

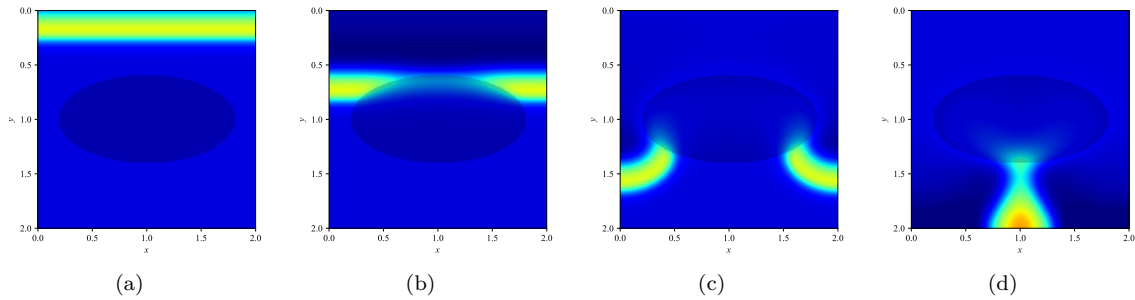


Figure 4.13: Snapshots of a wave passing through a large ischemic region, but has room to go around. Minor axis length,  $a = 0.4$ , major axis length,  $b = 0.8$ .

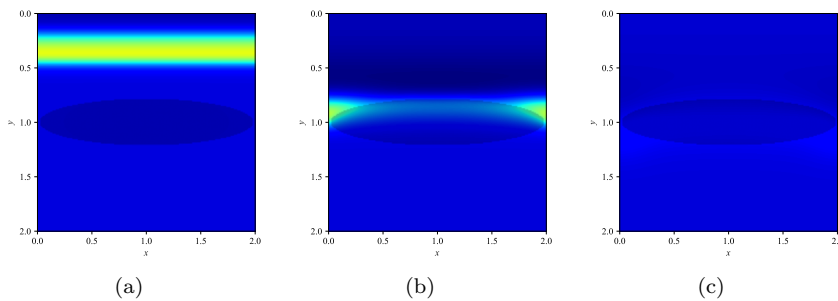


Figure 4.14: Snapshots of a wave passing through a large ischemic region. Minor axis length,  $a = 0.21$ , major axis length,  $b = 0.97$ .

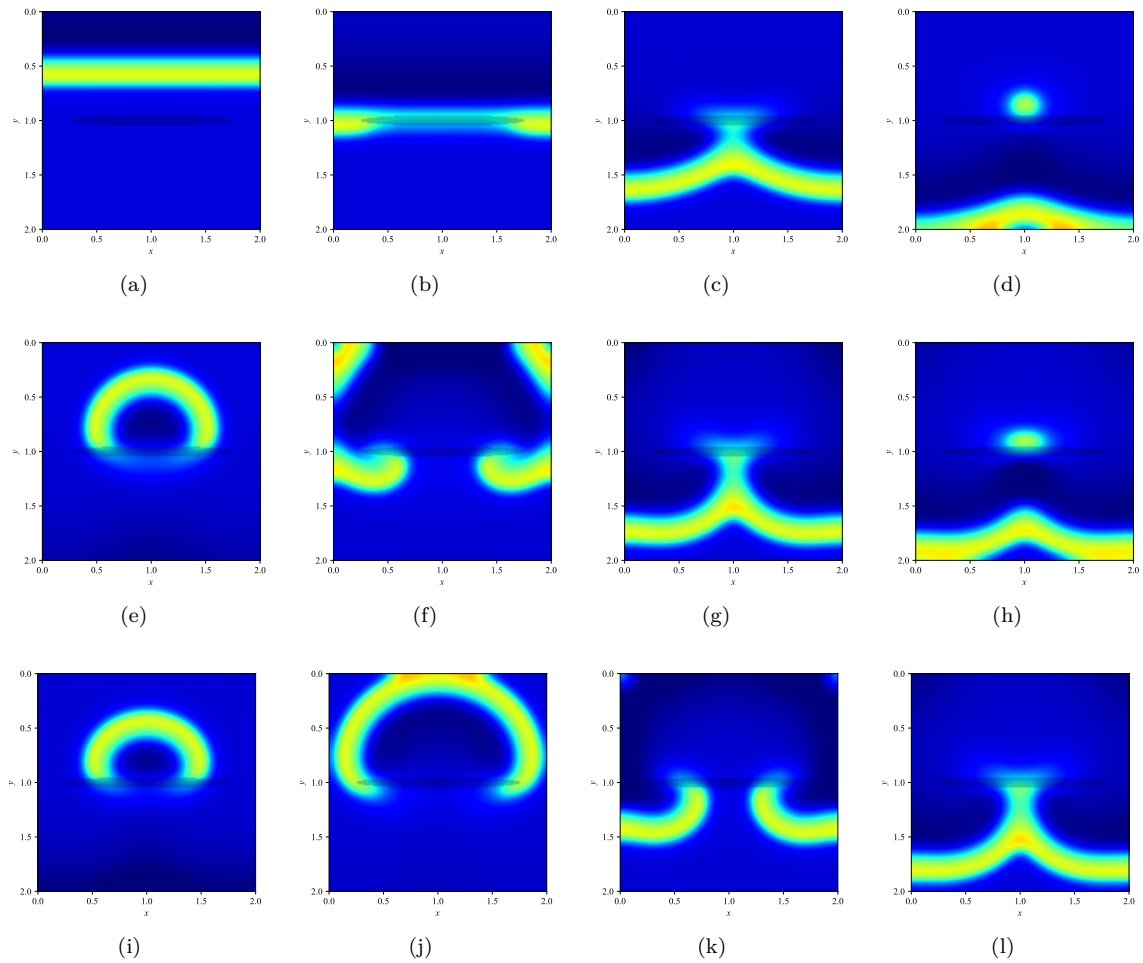


Figure 4.15: Snapshots of a wave of excitation travelling towards the ischemic region, then producing a reflected wave which turns into two spiral waves. Minor axis length,  $a = 0.05$ , major axis length,  $b = 0.75$ .

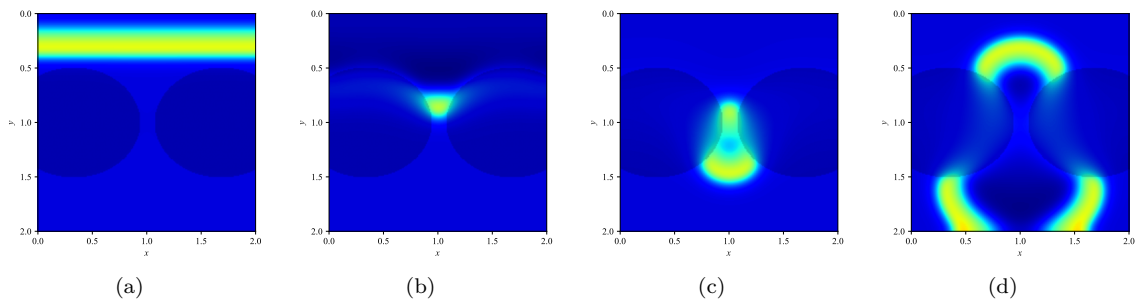


Figure 4.16: Snapshots of a wave traveling through an isthmus resulting in a reflection. Minor axis length,  $a = 0.5$ , major axis length,  $b = 0.6$ .

Figure 4.15 shows the creation of two spiral waves from a reflection. To explore where these three cases: pass, block, and reflection occur, simulations were performed for every possible ellipse size that fits inside of the domain. After each simulation, a tolerance test was performed to detect any persisting activities such as reflections and spiral waves. The test checks the level of activity in the first two thirds of the domain in the  $y$ -direction after three quarters of the simulation has been complete. From there, the tolerance test determines if the result is a pass, block, or reflection. The results after running simulations for every discretized ellipse size (with a maximum radius being the size of the domain) are shown in Figure 4.17. In Figure 4.17, there are two regions where reflections occur. The first region (marked red in Figure 4.17) is where spiral waves occur. In the second region (marked black in Figure 4.17) reflections occur from a wave travelling through an isthmus—a narrow path or region—and exiting into a larger excitable region which causes a reflection to propagate through the isthmus in a retrograde fashion (see Figure 4.16). For a more in depth explanation of this mechanism, see [11].

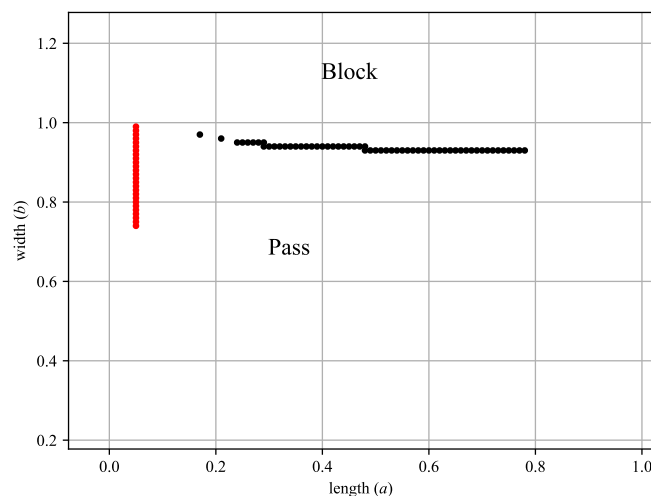


Figure 4.17: Where each type of behavior resides in  $a$ - $b$ (length-width) parameter space for a single ellipse. Spiral waves are marked with red and reflections from an isthmus are marked with black.

The region labeled “Block” in Figure 4.17, above the two regions where reflections occur, is where complete block occurs. The inexcitable region becomes too large for the wave to reach the distal side. The region marked “Pass” in Figure 4.17 are the  $a$  and  $b$  parameters that result in a pass.

Next, a second inexcitable region is placed in the domain. The two regions are identical ellipses, where the two ellipses are centered on the lines which trisect the domain (in the  $x$ -direction) into three equal part, and are centered in the  $y$ -direction. With the introduction of the second ellipse, spiral waves becomes more robust, meaning they appear more often than with a single heterogeneity. When the two heterogeneities become large enough a block occurs much like in Figure 4.14, and when the regions are small or spaced far enough away from each other, a pass occurs. There is a slight difference when a pass occurs now. The wave can either have a brief delay and return to its original state similar to Figure 4.12 (labeled as “Pass(I)” in Figure 4.23), or the wave is blocked on the sides allowing it to “loop” around the region but then is blocked again. Figure 4.18 shows an example of this and is labeled as “Pass(II)” in Figure 4.23. The reflections for long and narrow ellipses, like in Figure 4.15, now produce two reflected waves (one for each region) and result in two spiral waves that persist similarly to a single ellipse. This is illustrated in Figure 4.19.

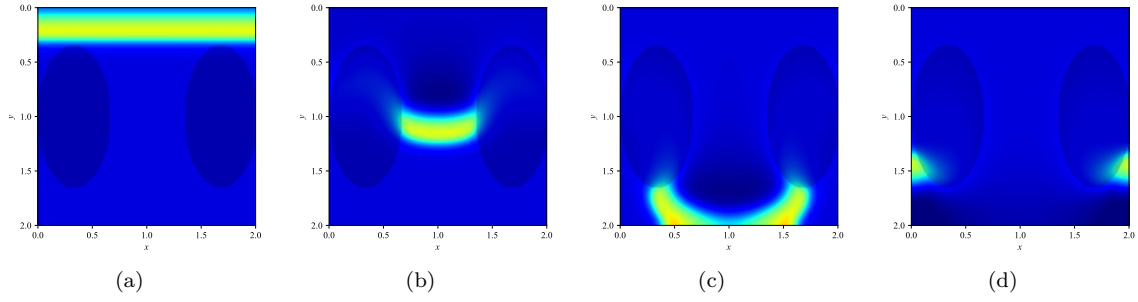


Figure 4.18: A simulated solution showing how the traveling wave tries to go around the two inexcitable regions but is blocked.  $a = 0.65$ ,  $b = 0.33$

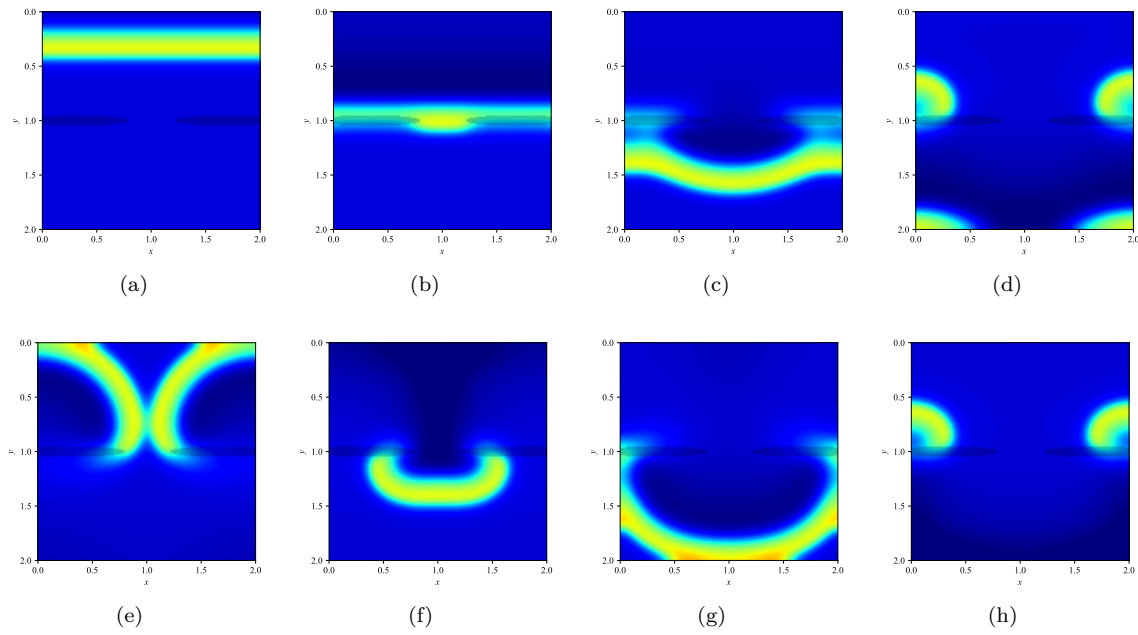


Figure 4.19: A simulated solution that leads to two reflections that turn into two spiral waves.  $a = 0.05$ ,  $b = 0.46$

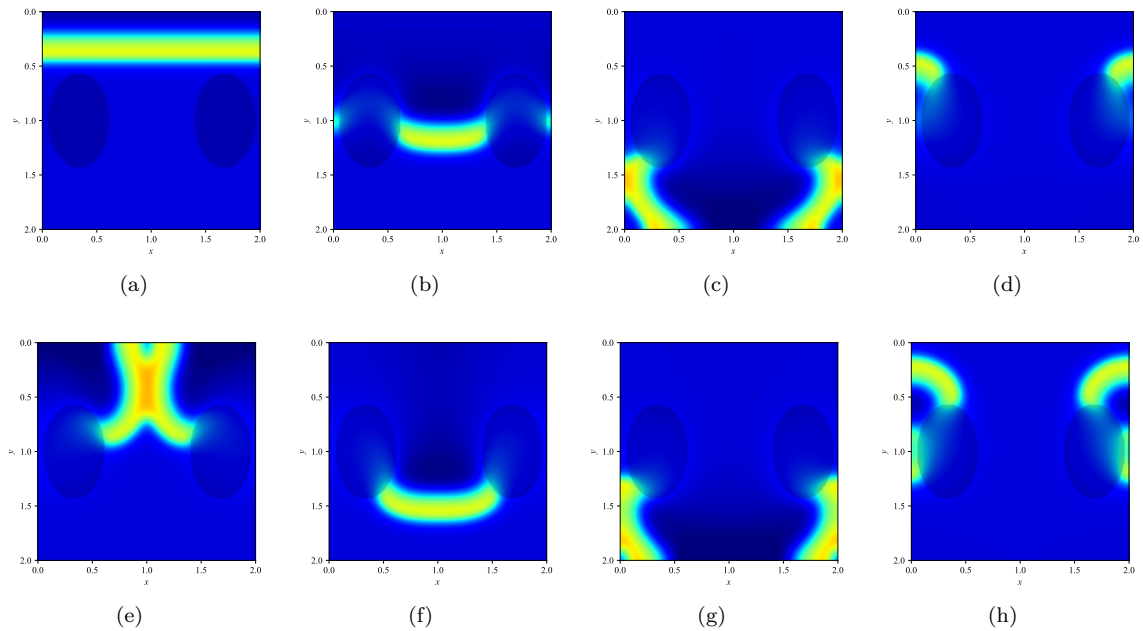


Figure 4.20: Snapshots showing the development of the spiral wave and how it travels around the inexcitable region.  $a = 0.43$ ,  $b = 0.28$ .

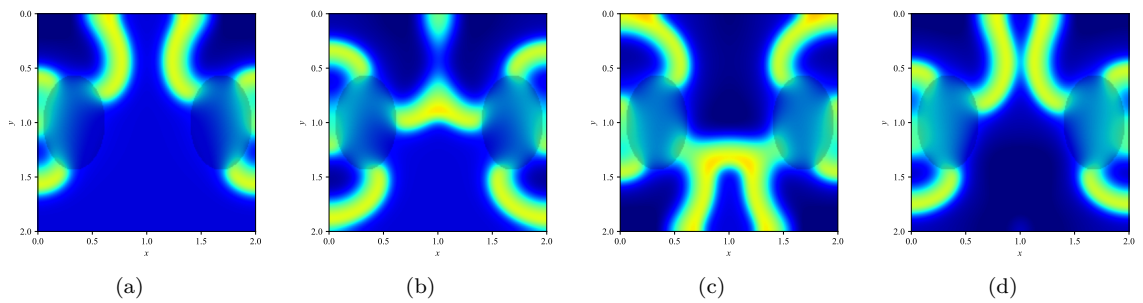


Figure 4.21: After making two loops around the ischemic region (Figure 4.20), a large amount of reflections occur with the pattern shown in the above figures.  $a = 0.43$ ,  $b = 0.28$ .

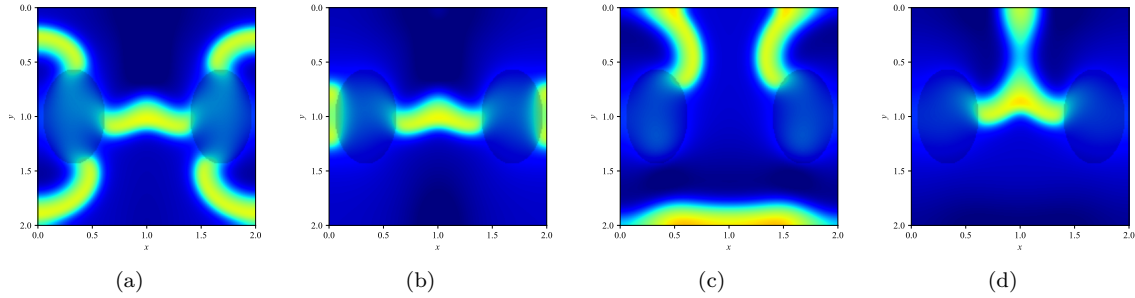


Figure 4.22: After the long sequence of reflections (Figure 4.21), the reflections ends and then the cycle restarts as it returns to two spiral waves traveling around the inexcitable regions (Figure 4.20).  $a = 0.43$ ,  $b = 0.28$ .

Figure 4.20 shows how the traveling wave interacts with two elliptical shaped, inexcitable regions that are almost large enough to result in block and are spaced far enough apart in the center to allow the wave to pass. This causes the wave to be blocked near the boundaries. This means the wave that is not blocked in the center of the domain can travel around the non-excitable region. Figure 4.20 shows how the waves travel around the non-excitable regions twice before reflections are generated. The creation of these reflections is seen in Figure 4.20(h). These reflections occur for a long period in a repeating pattern illustrated in Figure 4.21. After this sequence of reflections ends, two spiral waves form again and the cycle restarts. Figure 4.22 shows the transition from the reflections in Figure 4.21 to two spiral waves similar to Figure 4.20.

Parameter values at which reflections for two ellipse-shaped inexcitable regions occur is plotted in Figure 4.23. Similar to the single non-excitable region, there is a region (marked red in Figure 4.23) where a single reflection from each inexcitable region turns into two persisting spiral waves and a region (marked black in Figure 4.23) where a few reflections can occur due to the wave passing through an isthmus (see Figure 4.16). However, there is a new region (marker blue in Figure 4.23) where reflections from the isthmus can result in spiral waves that lead to more reflections from the isthmus (see Figures 4.20, 4.21, 4.22).

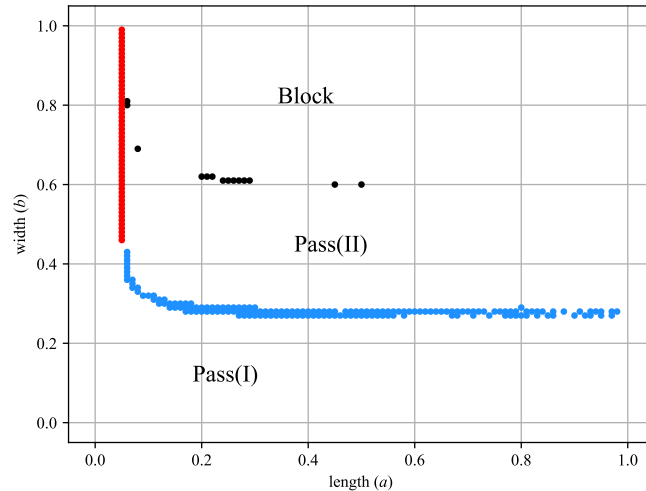


Figure 4.23: Where each type of behavior resides in  $a$ - $b$ (length-width) parameter space for two ellipses. Spiral waves are marked with red, reflections from an isthmus are marked with black, and combinations of spiral waves and reflections from an isthmus are marked with blue.

## 5 Conclusion

In this study, we examine the ML model and explore its behavior in an extended spatial setting and how adding regions of non-excitable media leads to exotic behaviors. When an inexcitable region is added, the system experiences delays which allow for wave reflections. These wave reflections have been linked to life-threatening arrhythmias via the one-dimensional spiral wave (which have been measured in isolated dog and sheep ventricular epicardial muscle [7]). Based on the physiological properties of myocardial ischemia, we set our modeled ischemic tissue, i.e. the inexcitable region, to be “smooth” ellipses and use more than one to model “random” distributions of non-excitable tissue. We find that reflections occur from multiple mechanisms, and each mechanism is distributed in groups. That is, in a region in parameter space where wave reflections occur from one mechanism of reflection, most of its “neighbors” elicit reflections from the same mechanism. Having more than one region appears to generate reflections and spiral waves more robustly. The ML model is an idealized model; using a more realistic model may lead to significant quantitative differences in where reflections occur in parameter space, and should be investigated further, but we expect that qualitative behaviors will be preserved.

## 6 Appendix

---

**Algorithm 1** Search for echo waves

---

```
 $\Delta v, \varepsilon \leftarrow 10^{-3}$ , machine epsilon  
 $v_1, w_1, w_2 \leftarrow$  fixed initial conditions (ICS)  
 $v_2 \leftarrow$  value that has 1 : 0 pattern  
 $\min_{v_2}, \max_{v_2} \leftarrow v_2, v_1$   
 $P \leftarrow 1 : 0$   
 $Best \leftarrow P$   
while  $\Delta v > \varepsilon$  do  
   $\vec{V}_1, \vec{V}_2 \leftarrow$  numerical solution for current ICS  
   $P \leftarrow$  peaks( $\vec{V}_1$ ) : peaks( $\vec{V}_2$ )  
  if  $P > Best$  then  
     $v_2 \leftarrow v_2 - \Delta v$   
     $\min_{v_2} \leftarrow v_2 - \Delta v$   
     $\max_{v_2} \leftarrow v_2 + 12\Delta v$   
     $\Delta v \leftarrow \Delta v/10$   
     $Best \leftarrow P$   
  continue  
  end if  
  if  $v_2 > \max_{v_2}$  then  
     $v_2 \leftarrow \min_{v_2}$   
     $\Delta v \leftarrow \Delta v/10$   
  end if  
   $v_2 \leftarrow v_2 + \Delta v$   
end while
```

---

---

**Algorithm 2** Count the number of time a solution goes above specified threshold

---

```
function PEAKS( $\vec{V}$ , threshold)  
   $n \leftarrow$  length of  $\vec{V}$   
  count  $\leftarrow 0$   
  for  $i \leftarrow 1$  to  $n$  do  
    if  $\vec{V}_i > threshold$  and  $\vec{V}_{i-1} \leq threshold$  then count  $\leftarrow count + 1$ 
```

---

---

```
    end if
  end for
  return count
end function
```

---

## References

- [1] W. J. Richardson, S. A. Clarke, T. A. Quinn, and J. W. Holmes, “Physiological implications of myocardial scar structure,” *Comprehensive Physiology*, vol. 5, pp. 1877–1909, Sep 2015.
- [2] C. Antzelevitch, J. Jalife, and G. Moe, “Characteristics of reflection as a mechanism of reentrant arrhythmias and its relationship to parasystole,” *Circulation*, vol. 61, p. 182–191, January 1980.
- [3] J. Jalife and G. Moe, “Excitation, conduction, and reflection of impulses in isolated bovine and serum cardiac purkinje fibers.,” *Circulation research*, vol. 49 1, pp. 233–47, 1981.
- [4] T. J. Lewis, *The Effects of Nonexcitable Regions on Signal Propagation in Excitable Media: Propagation Failure and Reflection*. PhD thesis, University of Utah, Salt Lake City, UT, 1998.
- [5] J. JALIFE, “The sucrose gap preparation as a model of av nodal transmission: Are dual pathways necessary for reciprocation and av nodal “echoes”?,” *Pacing and Clinical Electrophysiology*, vol. 6, no. 5, pp. 1106–1122, 1983.
- [6] C. Morris and H. Lecar, “Voltage oscillations in the barnacle giant muscle fiber,” *Biophysical journal*, vol. 35, pp. 193–213, Jul 1981.
- [7] J. M. Davidenko, A. V. Pertsov, R. Salomonsz, W. Baxter, and J. Jalife, “Stationary and drifting spiral waves of excitation in isolated cardiac muscle,” *Nature*, vol. 355, pp. 349–351, Jan 1992.
- [8] L. D. Weise, M. P. Nash, and A. V. Panfilov, “A discrete model to study reaction-diffusion-mechanics systems,” *PloS one*, vol. 6, no. 7, pp. e21934–e21934, 2011.
- [9] A. T. Winfree and S. H. Strogatz, “Organizing centres for three-dimensional chemical waves,” *Nature*, vol. 311, pp. 611–615, Oct 1984.
- [10] B. Ermentrout and J. Rinzel, “Reflected waves in an inhomogeneous excitable medium,” *SIAM Journal of Applied Mathematics*, vol. 56, pp. 1107–1128, 1996.
- [11] D. S. Auerbach, K. R. Grzda, P. B. Furspan, P. Y. Sato, S. Mironov, and J. Jalife, “Structural heterogeneity promotes triggered activity, reflection and arrhythmogenesis in cardiomyocyte monolayers,” *The Journal of Physiology*, vol. 589, no. 9, pp. 2363–2381, 2011.
- [12] B. Ermentrout, *Simulating, Analyzing, and Animating Dynamical Systems: A Guide to XPPAUT for Researchers and Students*. Software, Environments and Tools, Society for Industrial and Applied Mathematics, 2002.